Asymmetric effects of a modelled tidal turbine on the flow and seabed

Ramírez-Mendoza, R.[a,b,*], Murdoch, L.[c], Jordan, L.B.[d], Amoudry, L.O.[a], McLelland, S.[e], Cooke, R.D.[a], Thorne, P.[a], Simmons, S.M.[e], Parsons, D.[e], Vezza, M.[f]

[a] *National Oceanography Centre, 6 Brownlow St., Liverpool, L3 5DA, UK*
[b] *CICESE, Carr. Eda.-Tij. No. 3918, Playitas, Eda., BC, 22860, México*
[c] *CFD People LTD, 38 Lyle Road, Airdrie, ML6 8NB, UK*
[d] *School of Engineering, Institute for Energy Systems, The University of Edinburgh, Edinburgh, EH9 3DW, UK*
[e] *University of Hull, Hull, HU6 7RX, UK*
[f] *University of Glasgow, Glasgow, G12 8QQ, UK*

Abstract

The extraction of power from the flow of water has become an important potential source of clean energy. In spite of significant interest in the interaction between energy extraction devices and water currents, comparatively little work has focused on flow asymmetry. Indeed, unusual wake behaviour and limits of turbine array efficiency have typically been attributed to boundary effects rather than the particular turbine geometry. The aim of the present study was to reveal the asymmetries in the hydrodynamic wake and the interactions with the sediment bed due to the presence of a hydrokinetic turbine. We combined: (i) computational fluid dynamics simulations; (ii) optical flow measurements from a series of flume experiments above a fixed rough bed; and (iii) acoustic measurements from a further series of flume experiments above a mobile sand bed. Results showed flow asymmetry due to the presence of the rotor which appeared to be related to the development of the wake and potentially to the gyre of the blades. Suspended sediments in the flume also exhibited asymmetrical characteristics due to the flow asymmetry. This imbalance in the flow field and sediment transport may decrease energy extraction efficiency in turbine arrays and also could have important environmental consequences.

Keywords: Energy, turbines, sediments, tide, CFD, PIV

*Corresponding author
Email address: rrafael@cicese.mx (Ramírez-Mendoza, R.)

1. Introduction

Interest in clean sources of energy as alternatives to fossil fuels has grown significantly in recent years. Solar, wind, hydrological, geothermal, biological and marine resources are all available to generate renewable energy. Amongst these, marine resources are expected to grow globally with installed capacity increasing from less than 25 MW/yr in 2013 to reach at least 2000 MW/yr by 2030 (Ellabban et al., 2014). Marine energy can be extracted in a number of ways: i) thermal differences (e.g. Finney, 2008), ii) salinity gradients (Brauns, 2009), iii) waves (Falnes, 2007), and iv) tides (Bahaj, 2013). The preferred methods of extracting energy from tides are tidal barrages or lagoons, relying on converting potential energy linked to tidal range; or tidal stream devices, relying on converting kinetic energy from tidal currents. Tidal stream devices thus aim to generate energy using similar systems as those used for wind turbines (Bahaj, 2013). The fluid dynamic efficiency of a single tidal stream turbine (TST), or arrays of turbines, has been the focus of a number of studies (e.g. Myers and Bahaj, 2005; Maganga et al., 2010; Stallard et al., 2013). One of the main concerns is the dynamics of the wake behind the TST because determines the recovery of the flow and thus the optimal spacing between turbines for maximum energy efficiency.

However, the wake of hydrokinetic turbines is not free of the effect of the bottom boundary layer. This is particularly the case in regions where the boundary layer occupies most of the water column due to fast-moving tidal currents and relatively shallow water depth (Prandle, 1982). Wakes may also interact with the sediment bed, resulting in modifications of the boundary layer (Möller et al., 2016), the wake itself (Chamorro et al., 2013), and the response of sediments (Hill et al., 2014, 2016; Ramírez-Mendoza et al., 2018). These changes can then lead to altered erosion and deposition patterns downstream of turbines or arrays, which may in turn affect the wake structure, impacting the efficiency of TSTs downstream and the stability of their foundations. The environmental consequences of an entire array of TSTs will therefore depend on the interactions

between downstream wakes and the sediment bed.

Characterising turbine wakes has relied on laboratory experiments (e.g., Myers and Bahaj, 2010; Stallard et al., 2015; Tedds et al., 2014; Stallard et al., 2015) and numerical modelling using computational fluid dynamics (e.g., Harrison et al., 2010; Daly et al., 2013; Batten et al., 2013). These studies have evolved from experiments with actuator disks (e.g., Myers and Bahaj, 2010) to experiments with multiple three-bladed turbines (e.g., Stallard et al., 2013), experiments with turbines interacting with a bottom boundary layer (e.g., Stallard et al., 2015; Möller et al., 2016; Simmons et al., 2018), and experiments including mobile sediment beds (e.g., Hill et al., 2014, 2016; Ramírez-Mendoza et al., 2018). Computational fluid dynamics models have been applied to the study of TSTs from the use of homogeneous flows (e.g., Mason-Jones et al., 2013) to the inclusion of vertical profiles and waves (e.g., Tatum et al., 2016).

Wake asymmetry has been reported in some cases (e.g., Myers and Bahaj, 2012; Stallard et al., 2013; Tedds et al., 2014; Stallard et al., 2015). This is an important feature of hydrokinetic turbine wakes as it can influence the spatial distribution and location of wakes thus potentially impacting on spacing between turbines and turbine array design. Wake asymmetry is typically absent from the TST parameterisations used in the ocean models applied to large-scale environmental assessment (e.g., Roc et al., 2013; Thiébot et al., 2015; Li et al., 2017), thus potentially impacting upon the veracity of modelled large-scale environmental impact predictions. This wake asymmetry has often been attributed to the interaction between turbine wake and flow boundaries (Stallard et al., 2013; Tedds et al., 2014; Stallard et al., 2015). However, wake asymmetry has rarely, if ever, been the main focus in these studies. Studies focusing on scour and interactions with bed forms (e.g., Hill et al., 2014, 2016) have had little, if any, focus on the asymmetry of bed changes. Overall, there is a gap in studies with the specific objective of characterising the wake asymmetry and how it impacts and interacts with the sediment bed, its boundary layer, and sediment resuspension.

The present investigation addresses this gap and focuses on a holistic dynam-

ical description of the wake of a model hydrokinetic turbine and its interaction with a mobile sediment bed. To this end, the present study combines for the first time (i) numerical simulations in a current boundary layer using the velocity-vorticity formulation of the Navier-Stokes equations, (ii) high-resolution measurements of velocity and turbulence in the wake of a turbine above a fixed rough bed using particle image velocimetry (PIV), and (iii) acoustic measurements of the evolution of a mobile sediment bed and suspended sediment downstream of a model turbine. We present the observational and modelling methods in the following section. Numerical results and flume observations are then reported in section 3, focusing on demonstrating a consistent wake behaviour.

2. Methods

In this study we will show that the TST creates asymmetry effects on the flow field and sediment bed and that these effects can be found with three different study methods: numerical modelling; high resolution flow field laboratory experiments; and the sediment dynamics characterisation resulting from the experiments. The following sections introduce the numerical modelling and experimental methods used. Figure 1 presents the overall coordinate system, the numerical domain, and the experimental setups. All distances are normalised to turbine diameters, where $x/D = 0$ is the longitudinal TST channel position, $y/D = 0$ the traverse channel position, and $z/D = 0$ the channel bottom and flume fixed bed position for the numerical domain and experiments. The only exceptions are the bed morphology measurements in which, for clarity, negative/positive values represent sediment erosion/deposition relative to the initial bed sediment layer. Cross-stream positive and negative positions are also referred to in the text as $y/D > 0$ and $y/D < 0$, respectively.

2.1. Numerical Modelling

A series of high-resolution computer simulations have been conducted using a modified Vorticity Transport Model (VTM) and a horizontal axis turbine with

three blades with aerofoil NACA 0012 (Jacobs et al., 1935), having aspect ratio 4.65 and a polynomial twist of 18.58° from root to tip. The position of the model turbine (rotor) in the computational domain is illustrated in figure 1a. The modified VTM provides a detailed representation of the fluid dynamics that takes place within the wake of a rotor or turbine. This is achieved by considering the temporal evolution of the vorticity and velocity of an incompressible fluid, via solving the *Vorticity Transport Equation*:

$$\frac{\partial \omega}{\partial t} + (\mathbf{v} \cdot \nabla)\omega - (\omega \cdot \nabla)\mathbf{v} = S_\omega \tag{1}$$

where ω is the flow velocity field defined as $\omega = \nabla \times \mathbf{v}$, $\mathbf{v}$ is the flow velocity, S_ω is the vorticity source, and the operators ∇, $\nabla\cdot$, $\nabla\times$ and ∇^2 are the gradient, divergence, curl and Laplacian, respectively. The vorticity transport equation results from taking the curl of the unsteady, incompressible Navier-Stokes equations:

$$\frac{\partial \mathbf{v}}{\partial t} + \mathbf{v} \cdot \nabla \mathbf{v} = -\frac{\nabla p}{\rho} + \nu \nabla^2 \mathbf{v} \tag{2}$$

$$\nabla \cdot \mathbf{v} = 0 \tag{3}$$

where p is pressure, ρ is the fluid density and ν is kinematic viscosity. The velocity field is then obtained from the vorticity field as a solution of the Poisson equation:

$$\nabla^2 \mathbf{v} = -\nabla \times \omega \tag{4}$$

In the limit of zero viscosity, the viscous term becomes non-zero only on surfaces that are immersed in the flow. The vorticity source term S_ω in equation 1 represents the shed and trailed vorticity arising from the blades of the turbine and can be written as in Brown and Line (2005):

$$S_\omega = -\frac{d\omega_b}{dt} + \mathbf{v}_b \nabla \cdot \omega_b \tag{5}$$

where ω_b is the bound vorticity associated with each blade of the turbine and $\mathbf{v}_b$ is the velocity of the lifting surface relative to the local fluid.

The vorticity transport model we use has been validated against observational data in Brown and Houston (2000) and Phillips (2010). Phillips compared VTM results with aircraft rotor data and empirical formulations. It has been used for rotor aircraft studies (e.g. Fletcher and Brown, 2008; Houston and Brown, 2003; Green et al., 2005), wind turbines (e.g. Fletcher and Brown, 2010; Scheurich et al., 2011; Scheurich and Brown, 2011), and tidal turbines (Vybulkova et al., 2016).

In tidal flow, the velocity of the current varies with depth. The current forms the hydrodynamic boundary layer near to the sediment bed in which the flow adjusts to the distance from the sediment bed. This is captured in the model by including a free stream vorticity field. The boundary conditions on all outflow boundaries are set to zero normal gradient for the vorticity field to represent a fully developed flow. At the inlet boundary the freestream vorticity distribution is specified, and the interaction of the flow with the sea bed is modelled by the method of images (see below). The turbine is assumed to be deployed in a water column deep enough so that water surface effects can be omitted from consideration except at the surfaces of the rotor plane and the sediment bed.

2.1.1. Ground Effect

The sediment bed poses a physical constraint on the evolution of the flow surrounding the hydrokinetic turbine. The velocity component normal to the sediment bed has to be zero at the sediment bed in order to represent the assumed impermeability of the surface. The wake near the ground plane behaves like there was another wake, its mirror image in the ground plane (Whitehouse and Brown, 2004). The effect of the presence of the sediment bed on the dynamics of the flow has therefore been modelled in the modified VTM using the method of images (Whitehouse and Brown, 2004), in which the dynamics of the wake is calculated by superposition of the actual wake and the mirror image. The simulation thus fulfils the condition of zero flow through the sediment bed.

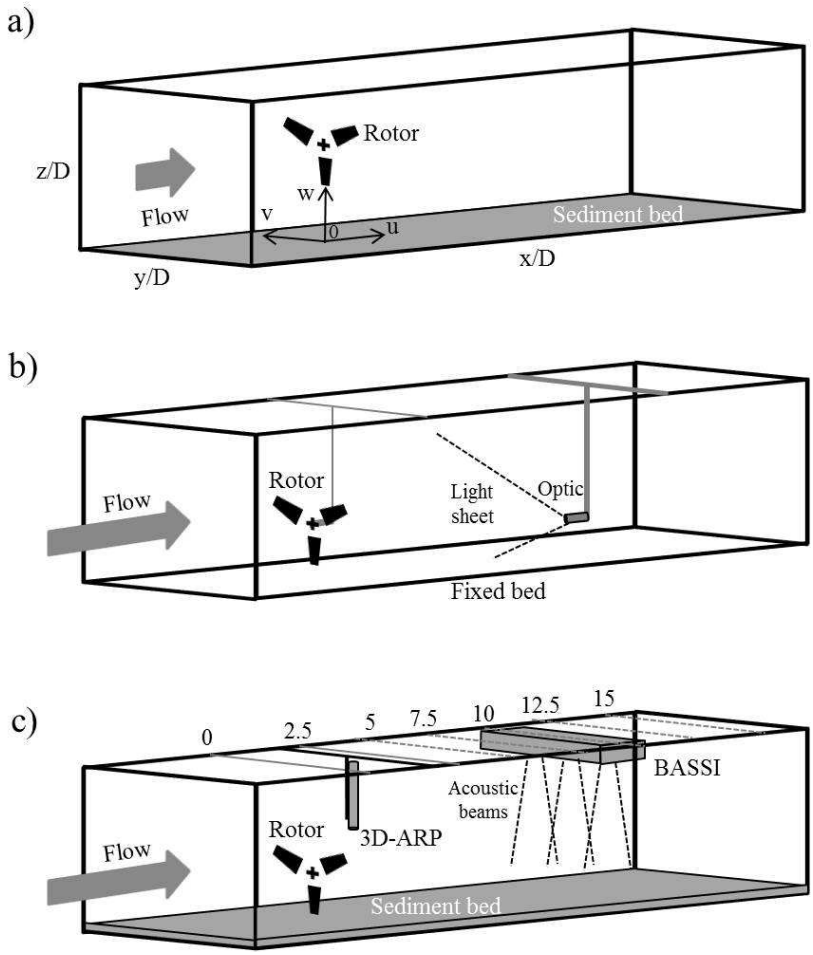

Figure 1: a) Computational domain for numerical modelling. Also is shown the coordinates system used for both numerical modelling and experiments. b) Channel schematic showing the position of the rotor relative to the optic, light sheet. c) Position of the 3D-ARP and locations where BASSI measurements were taken (dashed grey lines). An example of the BASSI module is shown at x/D =10 location. The drawings are not to scale.

2.1.2. Sediment motion

When a blade tip vortex approaches the sediment bed, the velocity that is induced parallel to the bed rises substantially. Individual vortices can create substantial unsteady shear stresses on the sediment bed, in some cases these unsteady stresses can exceed twice their time-averaged values (Lee et al., 2001). Initiation of sediment motion from the sediment bed is modelled within the modified VTM by postulating the existence of a threshold value of the shear stress at the sediment bed that has to be exceeded in order to initiate motion of sediment particles. This threshold for motion is given via a dimensionless critical bed shear stress, θ_c, following van Rijn (2007) which gives this critical bed shear stress as an empirical function of particle size, and which is valid for $4 \leq d^* < 10$, corresponding to a median sediment diameter, d_{50}, approximately between 0.22 mm and 0.54 mm, i.e. medium to coarse sand:

$$\theta_c = 0.14(d^*)^{0.64}, \tag{6}$$

where

$$d^* = d_{50}\left[\left(\frac{\rho_s}{\rho_w} - 1\right)\frac{g}{\nu^2}\right]^{1/3} \tag{7}$$

is the dimensionless sediment size (Miller et al., 1977), ρ_s is sediment density (2650 kg·m^{-3}), ρ_w is fluid density (1020 kg·m^{-3}), g is the gravity acceleration (9.8 m·s^{-1}) and, as mentioned above, ν is kinematic viscosity (1×10^{-6} m^2·s^{-1}). Sediment particles are assumed to leave the sediment bed when the bed shear stress exceeds the critical value, i.e. $\theta \geq \theta_c$, with θ the dimensionless bed shear stress:

$$\theta = \frac{\tau_b}{(\rho_s - \rho_w)gd_{50}} \tag{8}$$

where τ_b is the magnitude of the bed shear stress. The amount of sediment either as suspended load or bed load is commonly related to the excess bed shear stress (e.g. Amoudry and Souza, 2011), which we define as:

$$\xi = \left(\frac{\theta}{\theta_c} - 1 \right), \text{when } \theta \geq \theta_c. \quad (9)$$

We take this excess bed shear stress as a proxy to indicate the impact of the turbine on the sediment bed. Higher values correspond to more sediment in motion.

2.2. Experimental Setup

All flume experiments were performed in the Total Environment Simulator (TES) at the University of Hull, UK. The TES is a recirculating flume that is 6 m wide and 16 m long. Within this space, a test channel with a width of 1.6 m and a length of 11 m was constructed (Fig. 1b). This channel size was chosen as a compromise between minimising sidewall effects and maintaining a small enough water volume to drive large enough currents. A water depth of 0.6 m was used during the experiments to ensure a rotor, with a diameter of 0.2 m, was sufficiently far from the water surface to prevent the wake expansion being restricted vertically by the free surface (Olczak et al., 2015). The experimental programme was designed to investigate the wake downstream from the TST. Flow conditioning was used at the inlet to ensure a steady flow of about 0.4 $\text{m}\cdot\text{s}^{-1}$. The scaled turbine is further described in section 2.2.1 and the overall experimental setup results in the following: a blockage ratio of 0.039, a Reynolds number (Re) of the flow of about 10^6, rotor diameter Re of 10^5, a blade chord based Re 15×10^3, and a Froude number of 0.22.

The results reported hereafter comprise those obtained from two separate series of experiments. The first series focuses on high-resolution measurements of the streamwise velocity and of the turbulent kinetic energy in the wake of the model turbine (described in the following section) above a fixed bed. This was achieved using Particle Image Velocimetry (described in section 2.2.2) and the fixed channel bed was constructed from marine plywood boards covered with a layer of sand (d_{50} =425 μm) fixed to a thin coat of varnish to maintain a surface roughness. The second series focuses on measurements of bed morphology and

suspended sediment concentration for the case of the model turbine positioned above a mobile sediment bed. This was achieved using acoustic instrumentation described in sections 2.2.3 and 2.2.4.

2.2.1. Scaled hydrokinetic turbine

The scaled rotor consisted of a three-bladed, horizontal-axis model hydrokinetic turbine designed at the University of Strathclyde. The rotor of the turbine is unshrouded, with a diameter D =0.2 m, and three blades with a NACA 0012 aerofoil shape (Jacobs et al., 1935) and a polynomial twist of 13° from root to tip. The turbine is assumed to be a constant speed device with fixed blade pitch of 4°. Additional details on the turbine are reported in the study and supplemental data by Simmons et al., 2018. The turbine was mounted on an 8 mm diameter shaft which was attached to a 32 mm diameter housing for a 25 W DC motor. The motor housing was attached to a 68 mm×6 mm solid fin which was supported from above (Fig. 2). The motor housing and vertical support were designed to minimise flow disturbance. An important parameter to measure the efficiency of a turbine is the tip speed ratio (TSR), which is the ratio between the circumferential velocity of the blade tips and the fluid flow speed. The motor was computer-controlled to ensure the turbine rotated with a TSR of 5.5. This value corresponds to the maximum of the power curve for the flow velocity used in the experiments and rotor data were collected to ensure the TSR of 5.5 was maintained. The rotor was positioned in the centre of the channel at ∼6.6 m downstream from the inlet.

2.2.2. Particle Image Velocimetry

A stereoscopic two camera, three-component, submersible, double-pulse laser Particle Image Velocimetry (PIV) system, manufactured by Dantec Dynamics, was used. The laser was mounted on a frame above the channel and the laser optic was positioned approximately 2 m downstream of the TST (i.e. 10 diameters downstream). Two 4 Mpixel digital cameras mounted on a three-dimensional traverse system and encased in a submersible housing were used. The sub-

Figure 2: Hydrokinetic turbine with The three blades measuring 0.2 m diameter used during the experiments of Particle Image Velocimetry and mobile bed.

mersible housing consisted of mirrors on either end to enable the cameras to view upstream and downstream positions within the channel looking through a clear Perspex channel wall. The system enabled imaging of an area of 0.444 m by 0.312 m, horizontal and vertical orientation respectively, and the cameras could be moved 0.58 m in the streamwise, 0.4 m in the cross-stream and 0.35 m in the vertical directions. A three-dimensional calibration, acquired using a multi-level target, was obtained so that the two camera images could be combined to derive the three instantaneous flow velocity components (u streamwise, v cross-stream and w vertical). The calibration was valid for all camera positions since the optics remained submerged and there were no changes in image refraction. The flow was seeded using Plascoat Talisman 20, a neutrally buoyant copolymer coating powder, which was wet-sieved to refine the size of the seeding to between 106 μm and 212 μm.

For the PIV experiments described herein, the rotor hub was positioned at 0.12 m above the bed (z/D =0.6). In order to capture the full extent of the near wake, three different streamwise positions for the cameras were used for PIV measurements. These had a longitudinal distance of ∼0.29 m. The positions overlapped which ensured the flow field was captured without any gaps in the data. Data in the cross-wise orientation of the channel were collected on planes located at $y/D = -0.25$ and y/D =0.25, allowing the full wake flow field to be captured. When data were collected either side of the centreline, the laser was moved off the centreline to a specific location to ensure that the area where data were being collected was fully illuminated by the laser light. The stereoscopic cameras were also moved the same distance to ensure the images remained in focus and data were collected for the correct area.

Data were collected for 107 seconds (limited by data storage capacity) at each position, at a sample rate of 50 Hz. The collected PIV image data were processed using Dantec Dynamics Dynamic Studio v4.15. The data were analysed using an adaptive PIV algorithm which used a grid spacing of 32×32 pixels, and a minimum interrogation area size of 16×16 pixels and a maximum interrogation area size of 32×32 pixels. This equated to a grid spacing of approximately

6.15×5.8 mm. Adaptive PIV was used as the processing algorithm as it adjusts the size of the interrogation area in relation to the seeding densities and flow magnitude and gradients within that area, therefore increasing the quality and resolution of the data produced compared to standard correlation techniques (Theunissen et al., 2007).

2.2.3. Bed morphology

For the experiments above a mobile sediment bed, a 0.1 m thin layer of sand of d_{50}=425 μm was placed at the bottom of the flume prior to it being filled with water up to 0.6 m depth. The pumps were then run to first generate a steady current until stabilisation of the sediment bed: i.e. ripples reached a morphologically stationary state. A Marine Electronics three dimensional sand acoustic ripple profiler (3D-ARP) with an accuracy of approximately two milimeters was then used to monitor changes in the sediment bed position (Thorne et al., 2018). The 3D-ARP takes three dimensional measurements of the bed using a 1.1 MHz pencil beam transducer. The transducer is mounted looking downward at a certain distance from the bottom and records the position of the bed from its acoustic echo in a circular area around the 3D-ARP. The two-dimensional circular map of the bed is obtained following a cycle: an acoustic beam is first emitted from the transducer to point on the perimeter of the measurement disk; a two axis stepping motor then modifies the angle of the acoustic beam in the vertical until a complete diameter or transect of the measurement circular area is completed in an arc of 150°; the motor then rotates 0.9° in the horizontal plane and collects another transect; the cycle ends when the full measurement circular area has been covered in 200 individual swaths, equivalent to 180° (Fig. 3).The measured backscatter profiles were processed using an algorithm to recognise the bottom echo relative to the transducer location.

During the experiments reported here, the 3D-ARP was mounted at 0.43 m downstream from the rotor (Fig. 1c) and the complete measuring cycle took about 12 minutes. Since the 3D-ARP measurement circular area was larger than the flume width, the analysis only focused on a smaller area of about 1.4 m^2

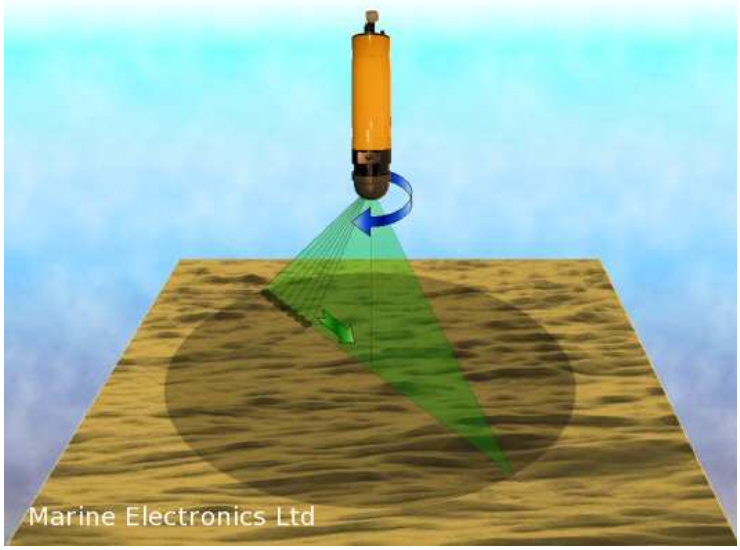

Figure 3: Schematic illustration of the acoustic ripple profiler sampling technique (www.marine-electronics.co.uk). Acoustic beams are emitted from the perimeter (black dots) and along a transect until a complete diameter is covered (green arrow and vertical shadded plane). Then the angle is modified to take another transect (blue arrow) and continues until the entire circular area of the bed is completed (dark shadow in the bottom).

in order to avoid contamination by wall reflections of the acoustic signal. The bed evolution was recorded with the scaled rotor hub at two different heights from the initial surface sediment bed layer, 0.15 m and 0.2 m, to observe the changes over periods of a few hours. At the end of the experiments a last 3D-ARP measurement was taken to record the final state of the bed. The 3D-ARP algorithm results are distances from the transducer to the bed which were converted to show the loss or gain of sediment relative to the initial bed sediment layer.

2.2.4. Suspended sediment concentration

Measurements of the sediments in suspension were obtained using an acoustical backscatter instrument called BASSI (Bedform and Suspended Sediment Imager). The BASSI consists of arrays of Acoustic Backscatter Systems, and each BASSI unit has five sets of three transducers at different frequencies, aligned to give a vertical profile of the backscattered signal from suspended sediment over

a 0.5 m transect (Moate et al., 2016; Thorne et al., 2018). An approximation to suspended sediment concentration, SSC, can be obtained after calibration of the transducers using either field samples or backscatter acoustic properties of the particles in suspension. In this investigation, the latter method was used following Thorne and Meral (2008), Moate et al. (2016) and Thorne et al. (2018). Three arrays were aligned to cover 1.5 m, almost the width of the channel. The transducers worked at alternate frequencies of 0.75, 1.25 and 2.5 MHz and recorded measurements at about 5 Hz sample rate for approximately 10 minutes. The profiles obtained by each transducer were time-averaged and after applying calibration three SSC profiles were calculated, from which a single averaged profile was obtained. The result is a vertical plane view of the SSC covering almost the flume width. The transducers were moved to five different locations in the streamwise direction to have the SSC in the far wake zone from the rotor (Fig. 1c).

3. Results

3.1. Numerical Modellling

The vorticity field induced by the presence of the device on the sediment bed has been modelled by the modified VTM. Overall, the wake achieved a quasi steady state after 13.4 rotor revolutions with one rotor revolution lasting 6.28 seconds of simulation time (28.5 hours run time). The results showed small changes after 20.2 rotor revolutions of a total of 36.8, and the average bed shear stress converged to a nearly constant value after about 16 rotor revolutions (data not shown).

Figure 4 illustrates the wake induced vorticity field downstream of the turbine described in section 2.1. Although purposely not directly the equivalent of any available commercial system, the turbine design places it in the mid-range of current design configurations of tidal stream turbines. Strong vortices bound to the rotor blades form a sequence of concentrated vortex filaments, yielding a helical structure to the wake as it convects into the flow downstream of the

turbine. The inflow velocity profile causes the helical structure to incline due to the vertical gradient of the inflow velocity. The inclination of the induced vorticity field contributed to its eventual disintegration into a cloud of vorticity fragments.

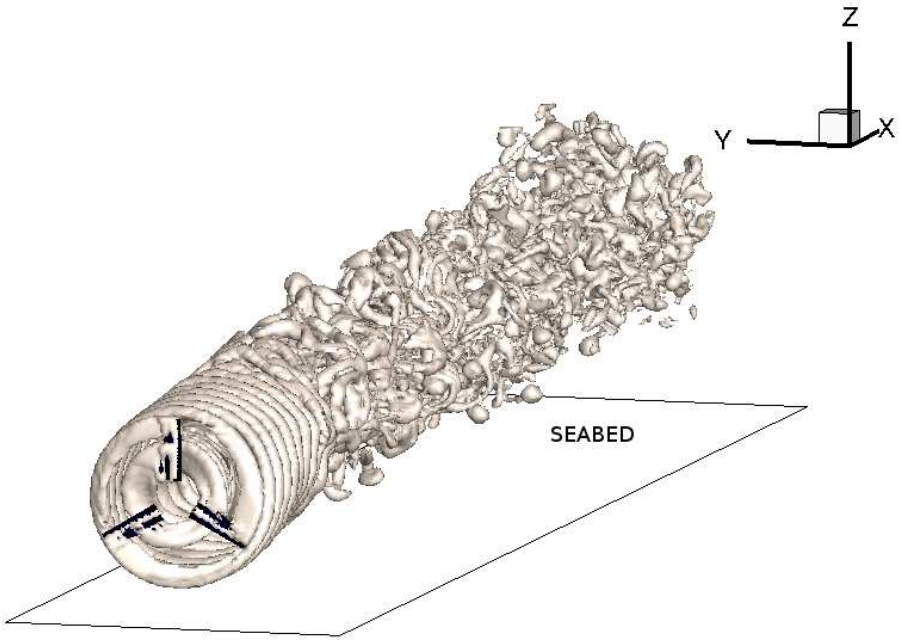

Figure 4: Illustration of the wake vorticity field in the computational domain.

Simulations were repeated for several positions of the rotor above the bed, all with the same inflow condition. The inclination angle of the vorticity loops in the helical structure downstream of the rotor is greater when the turbine is closer to the sediment bed. For all studied rotor positions the vorticity is elevated from the sediment bed by the flow further than one diameter downstream of the rotor. The vorticity induced by the flow affects the velocity near the sediment bed, which is crucial for the uplift of sediment into suspension. The near bed flow velocity magnitude normalised to the rotor diameter, $V = \sqrt{u^2 + v^2 + w^2}/D$, at z/D=0.01 above the sediment bed for different rotor positions, is shown in figure 5. The excess shear stress on the sediment bed is driven by the velocity just above the bed. Figure 6 shows the spatial distribution of the excess bed

shear stress also for the studied positions of the rotor above the sediment bed.

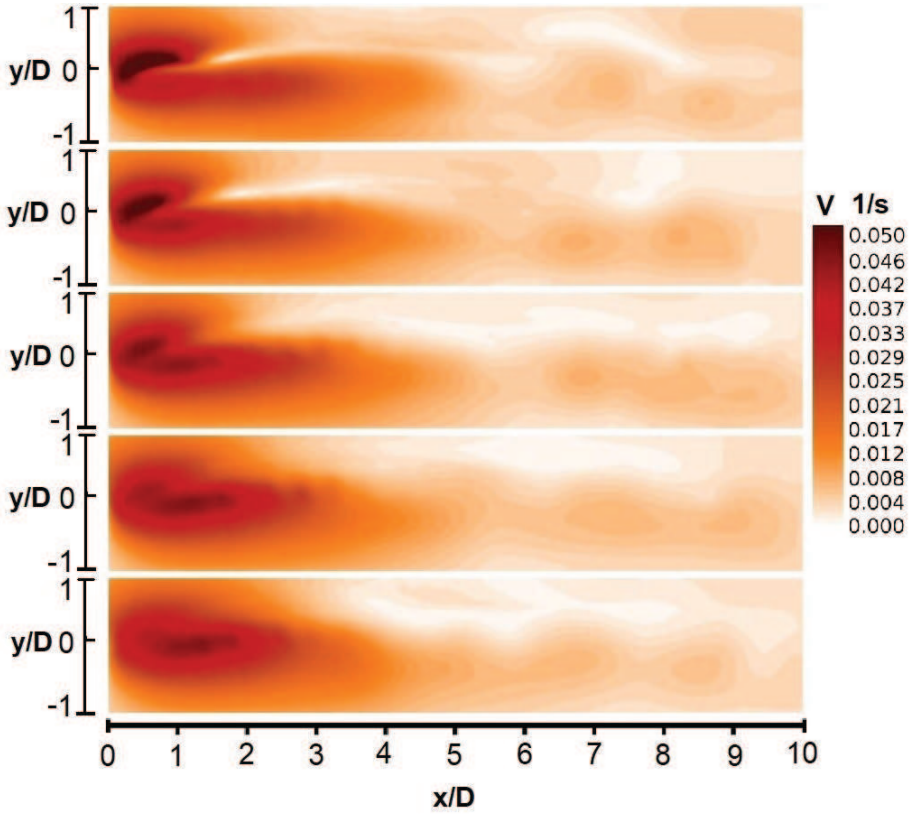

Figure 5: Normalised near bed velocity at z/D=0.01 downstream of the hydrokinetic turbine induced by a fully developed wake.The position of the rotor (and the centreline) is at x/D=0, y/D=0 and, from top to bottom z/D=0.525, 0.55, 0.575, 0.6 and 0.625 above the bed.

The excess bed shear stress contains high values in the region immediately downstream of the rotor for all investigated positions of the turbine. The maximal value of the excess bed shear stress depends on the proximity of the turbine to the sediment bed. In particular, when the rotor was closer to the sediment bed the excess bed shear stress reached the highest values (white colour in first panel on figure 6). However, the excess bed shear stress effect covered larger areas with increasing distance between rotor and bed. There is also an asymme-

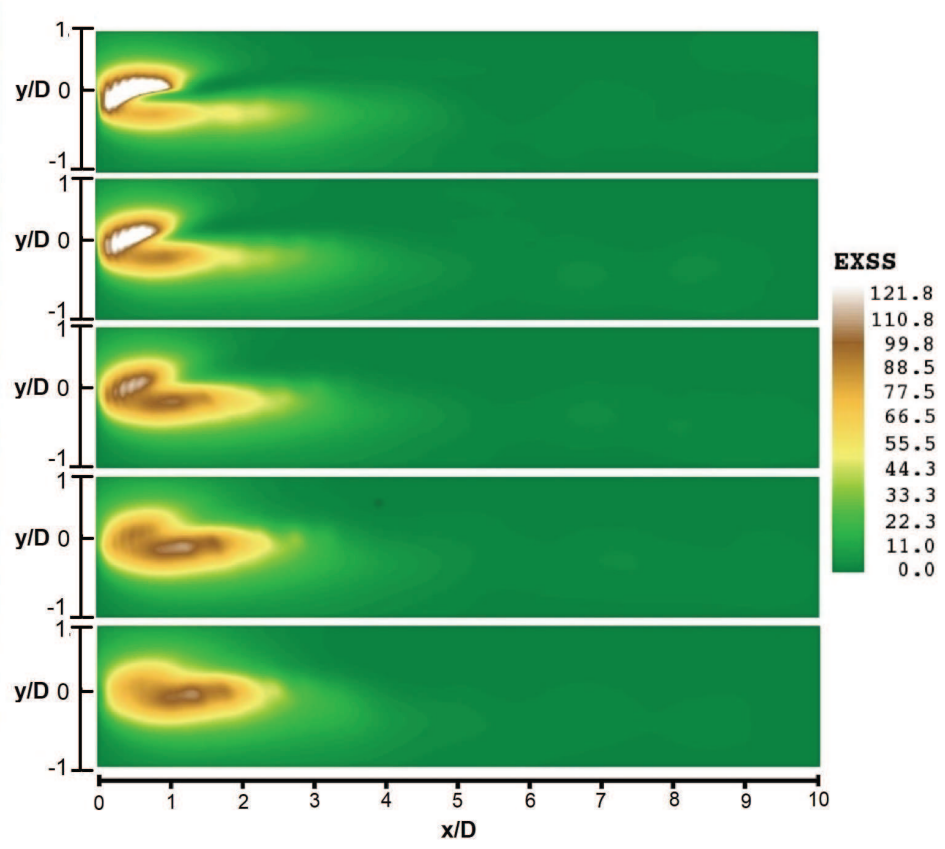

Figure 6: The excess bed shear stress downstream at $z/D=0.01$ of the hydrokinetic turbine induced by a fully developed wake, illustrating the asymmetry of the exposed area of the sediment bed. The position of the rotor (and the centreline) is at $x/D=0$, $y/D=0$ and, from top to bottom $z/D=0.525$, 0.55, 0.575, 0.6 and 0.625 above the bed.

try of the excess bed shear stress along the y axis with the highest magnitudes to the positive side, $y/D > 0$. This asymmetry reduces with increasing distance between rotor and bed, but it still remains evident at z/D=0.625.

3.2. Hydrodynamics from PIV experiments

The measurements for this section were collected above a fixed rough bed. The profile of the free-stream flow speed (U_p) when the turbine was not present in the channel is shown in figure 7. The profile is time averaged over the full capture period (107 seconds), and spatially averaged between x/D=0 and x/D=4 downstream of the rotor, on the centreline. Figure 8, with the turbine in the flume, shows flow structure maps for the streamwise u velocity component at $y/D = -0.25$ (Fig. 8a), y/D=0.25 (Fig. 8b) and the difference between both sides (Fig. 8c). There is a less well-defined wake on the y/D >0 side because the wake structure dominates the interaction with the near-bed flow due to the slower near-bed flow below the wake from x/D=2.5 downstream. In addition, there is increasing transverse asymmetry in the lower wake as the distance downstream increases which is clearly seen in figure 8c.

The velocity deficit profiles at x/D=2, 3 and 4 (downstream) for both sides y/D±0.25 and their corresponding differences are shown in figure 9. Differences were calculated as the positive side (y/D =0.25) minus the negative side (y/D = −0.25). The streamwise velocity deficit, U_d is a non-dimensional number that is relative to the free-stream flow speed through the channel U_p, and the wake velocity U_x:

$$U_d = 1 - \frac{U_x}{U_p} \tag{10}$$

The results showed significant differences in the wake velocity deficit on either side of the channel centreline, $\pm y/D$. There was a slightly greater acceleration of flow beneath the wake on the y/D <0 side of the channel (Fig. 9a). This acceleration resulted in negative velocity deficit values near the bed. At x/D =3 there was a significant velocity recovery although differences between

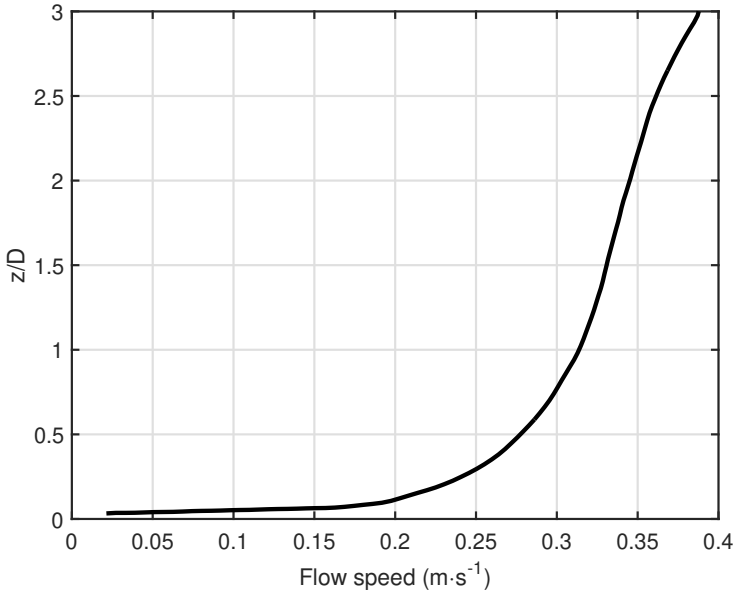

Figure 7: Profile plot of the mean streamwise flow, U_p, in the channel without the tidal stream turbine present.

cross-stream sides increased below the rotor elevation (Figs. 9d-9f). Nevertheless, there is a wake recovery close to the bed at $x/D = 4$ with higher velocity deficit on the $y/D > 0$ side of the centreline (Fig. 9c).

Turbulent kinetic energy k was also obtained from PIV measurements as:

$$k = \frac{1}{2}\left(\overline{u'^2} + \overline{v'^2} + \overline{w'^2}\right) \tag{11}$$

where u',v', and w' denote fluctuations of the streamwise u, cross-stream v and vertical w velocity components, respectively. The turbulent kinetic energy shows an increase in magnitude in two thin regions of flow extending downstream from the location of the TST rotor tips (Figure 10). These then expand vertically and increase in magnitude with distance downstream. The expansion in the $y/D > 0$ side appeared from the near wake region in a circular area at a $x/D = 1$ location. This area does not exist in the $y/D < 0$ side. However, the

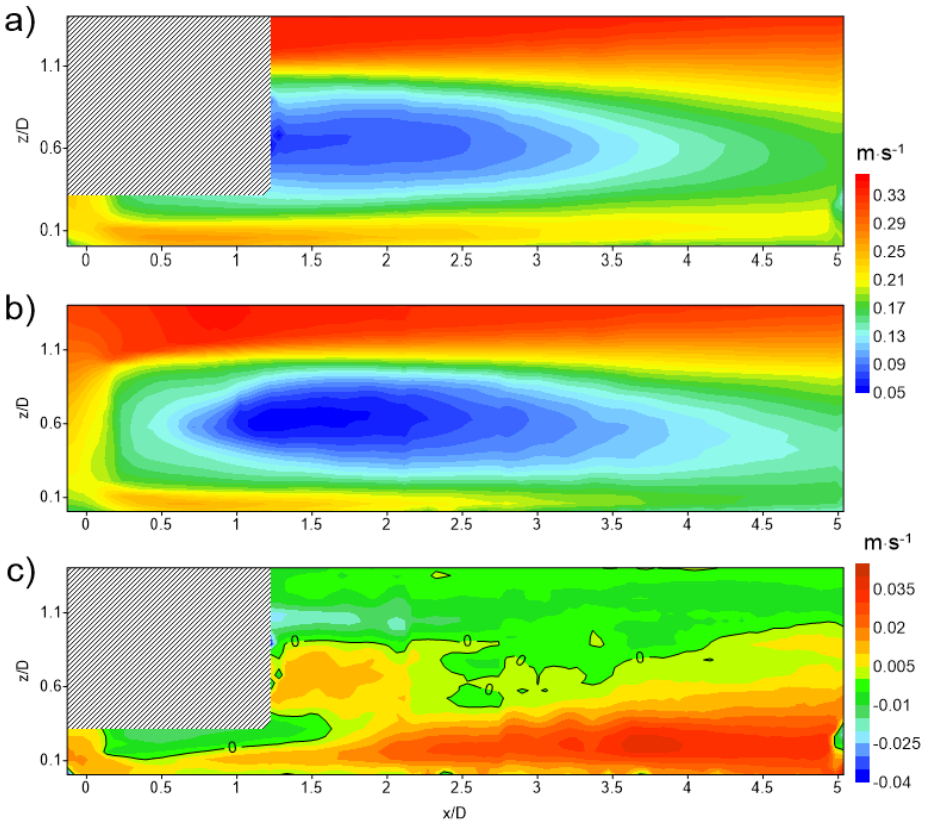

Figure 8: Flow structure maps for streamwise velocity component u with the turbine in the flume: a) $y/D = -0.25$ and, b) $y/D = 0.25$, and c) difference of (a) minus (b). Scales on the axes are normalised to rotor diameters (0.2 m). Areas covered by upward diagonal line shading indicate areas where data could not be collected as the camera image was obstructed by the rotor and housing or the flume support structure.

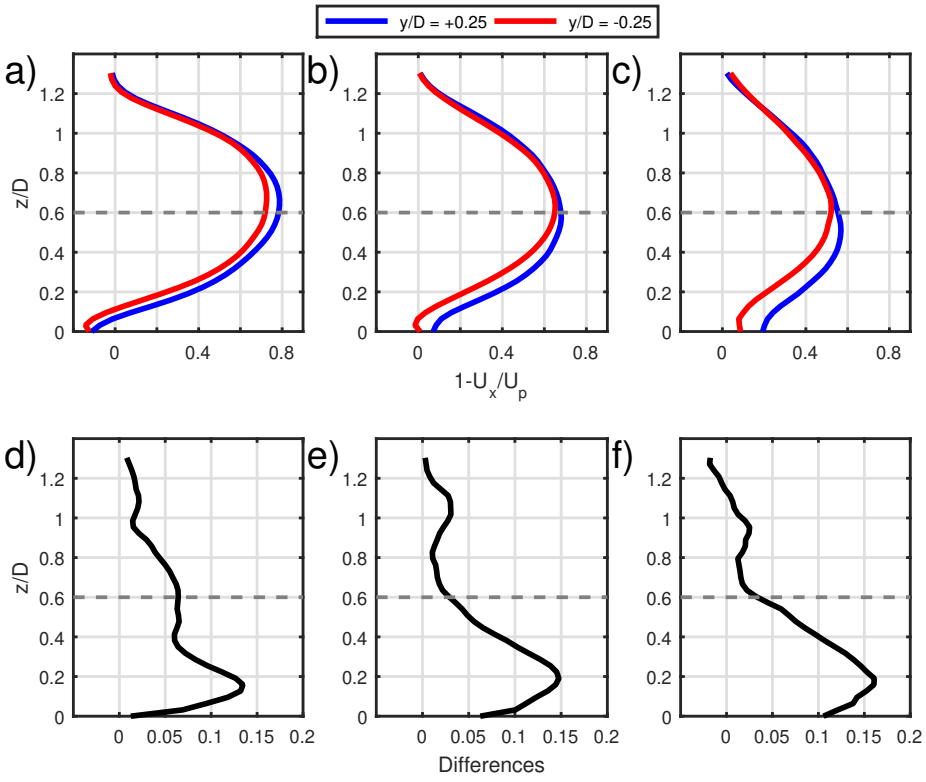

Figure 9: Velocity deficit $(1 - U_x/U_p)$ profiles at different downstream positions from the turbine: a) x/D =2, b) x/D =3, and, c) x/D =4. Lower panels show differences between profiles at the corresponding positions as in upper panels. Scales on the vertical axes are normalised to rotor diameters (0.2 m). Rotor is positioned at z/D=0.6 (dashed line).

areas of high turbulent kinetic energy at the far wake from about x/D=2 can be vertically distinguished. High magnitudes prevailed in the upper half at both sides but slightly highest values were present in the y/D>0 side.

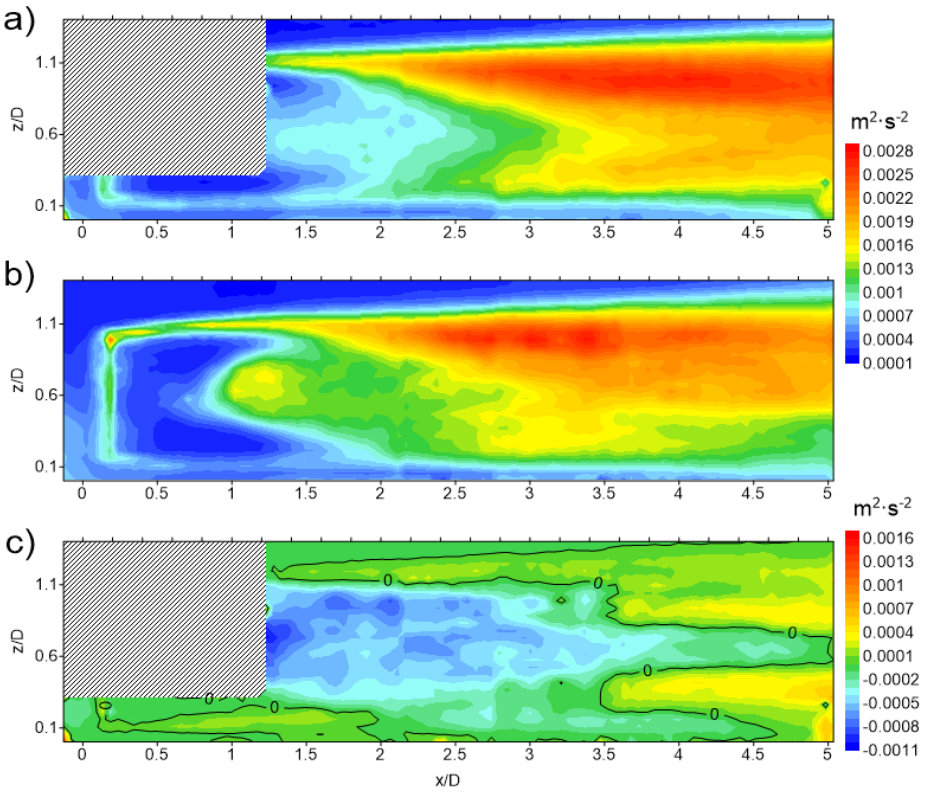

Figure 10: Flow structure map for turbulent kinetic energy k at: a) $y/D = -0.25$, b) y/D =0.25, and c) difference between (a) minus (b). The axes are normalised to rotor diameters (0.2 m). Areas covered by upward diagonal line shading indicate areas where data could not be collected as the camera image was obstructed by the rotor and housing or the channel support structure.

The corollary of these observations is that the asymmetric acceleration of flow below the rotor tip causes lateral differences in the shear between the wake and the flow beneath the turbine. This causes greater turbulence production in the lower wake on the negative side of the centreline, which increases mixing within the flow, leading to faster wake recovery and therefore a reduced recovery length. This is supported by turbulence intensity (streamwise component of the turbulent kinetic energy), I, exhibiting a significant decay from the pos-

itive, y/D=0.25, to the negative side, y/D= −0.25, of the centre line (Figure 11). Note that upstream values of I are in the expected value of ∼10%. The turbulence intensity was calculated as:

$$I = \frac{\sqrt{\overline{u'^2}}}{U_x} \tag{12}$$

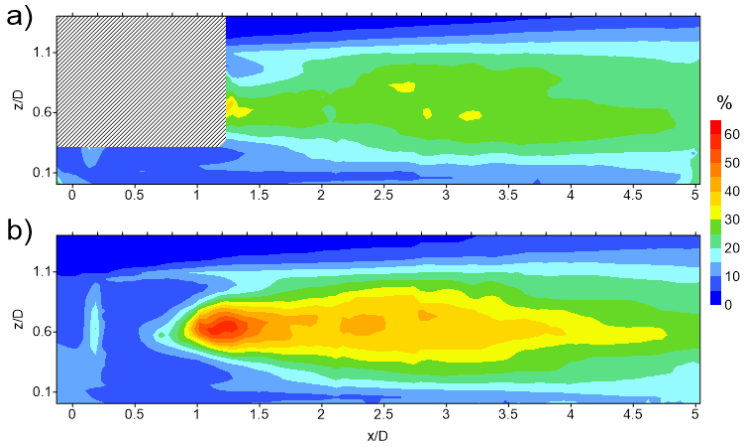

Figure 11: Turbulence intensity, I, based on equation 12 at: a) y/D= −0.25, b) y/D=0.25. The axes are normalised to rotor diameters (0.2 m).

3.3. Sediment dynamics

The bed morphologies before and after installation of the TST and their differences are shown in figure 12. At the end of the stabilisation period (five days) shown in figure 12a, small linguoid ripples were formed which correspond to high energy environments (Reineck and Singh, 1975). Even though there is a transverse asymmetry in the sediment bed prior to introducing the TST, it is smaller that differences due to the presence of the TST. This effect is likely due to some imperfections of the initial sediment bed since there was not important cross-stream differences in the flow (see figure 13 in Ramírez-Mendoza et al., 2018). A significant rearrangement of the sediment bed is clearly seen after the installation of the modelled TST (Fig. 12b). In particular, an important scour (shown in light blue in figure 12b) behind the rotor is present at the centreline

from x/D=0 to x/D=1 in the streamwise direction. The erosion expands into a "V" shape to $y/D = -2$ and up to y/D=3 in the cross-stream direction. At the centreline and beyond x/D=1 in the streamwise direction, an area of important deposition (green to red in figure 12b) is present and represents one of the regions with maximum height within the measured area. A particularly interesting feature of this structure, further discussed in section 4, is the asymmetric form which shows a skew to the $y/D>0$ side of the flow. Scour on this side of the channel, $y/D>0$, is generally more important than that on the negative side, $y/D<0$. There are other areas with important sediment deposition at the far wake (at x/D =5, $y/D = -2.8$) and upstream (at $x/D = -0.5$, $y/D = -2$) with the latter the most important of the measured area. Figure 12c shows that the most important changes between both conditions occurs in the $y/D>0$ side where areas of significant deposition and erosion can be distinguished.

Suspended sediment concentration, SSC, measured by the BASSI instrument showed transverse differences in the far wake region. Figure 13 shows SSC vertical cross-stream ratio C/C_o, where C and C_o denote conditions with and without the rotor, respectively, at along channel locations from x/D=5 to x/D =15. Results are plotted in a base 10 logarithmic scale for a better observation of the differences. This means that a value of 1.5 indicates that SSC with the rotor in the flume was 30 times higher than SSC without the rotor. A zero value results if no change occur between both conditions while a -0.5 value means that SSC diminished (0.31) with the rotor in the flume. The figure shows a non-uniform cross-stream suspended sediment distribution in all cases. Two maxima can be identified at each side in all panels but at non-symmetrical locations. In three cases, x/D =7.5 to 12.5, these maxima were located consistently at nominally $y/D = -0.5$ and y/D =1.5. For the other cases the maxima for $y/D>0$ side varied its location. The closest, x/D=5, and farthest, x/D =15, presented maxima at y/D=0.5 and y/D=1, respectively. On these same x/D locations but on the other side, $y/D<0$, maxima were found at the same $y/D = -1.5$ location.

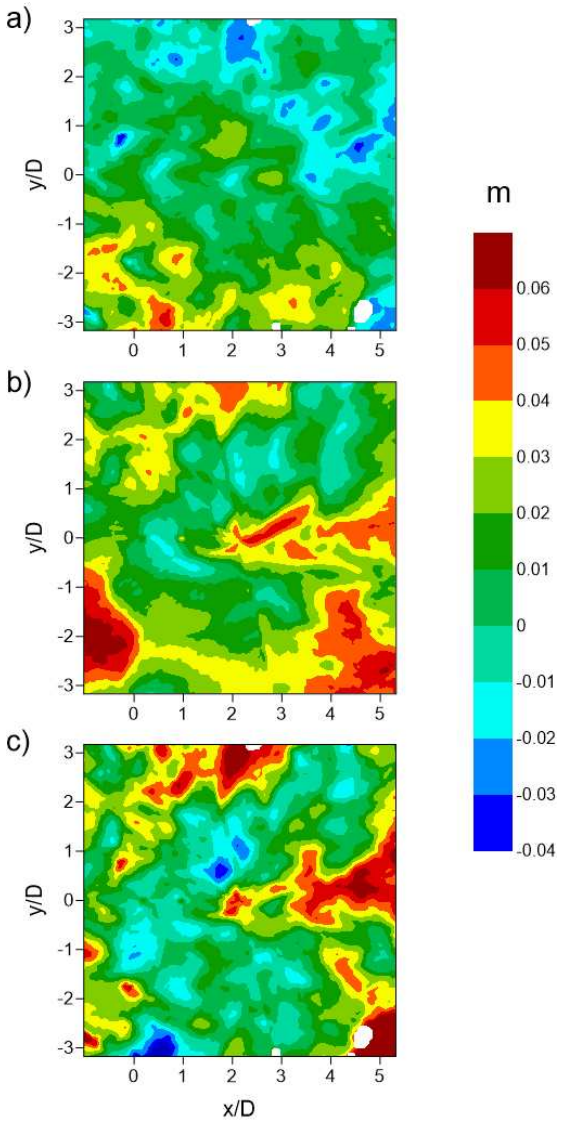

Figure 12: Sediment height relative to the initial surface sediment bed (0.1 m above the flume floor). a) Morphology after bed stabilisation without the rotor and before the experiments. b) Morphology at the end of the experiments with the rotor installed at x/D =0, y/D =0 location. c) Difference between both conditions.

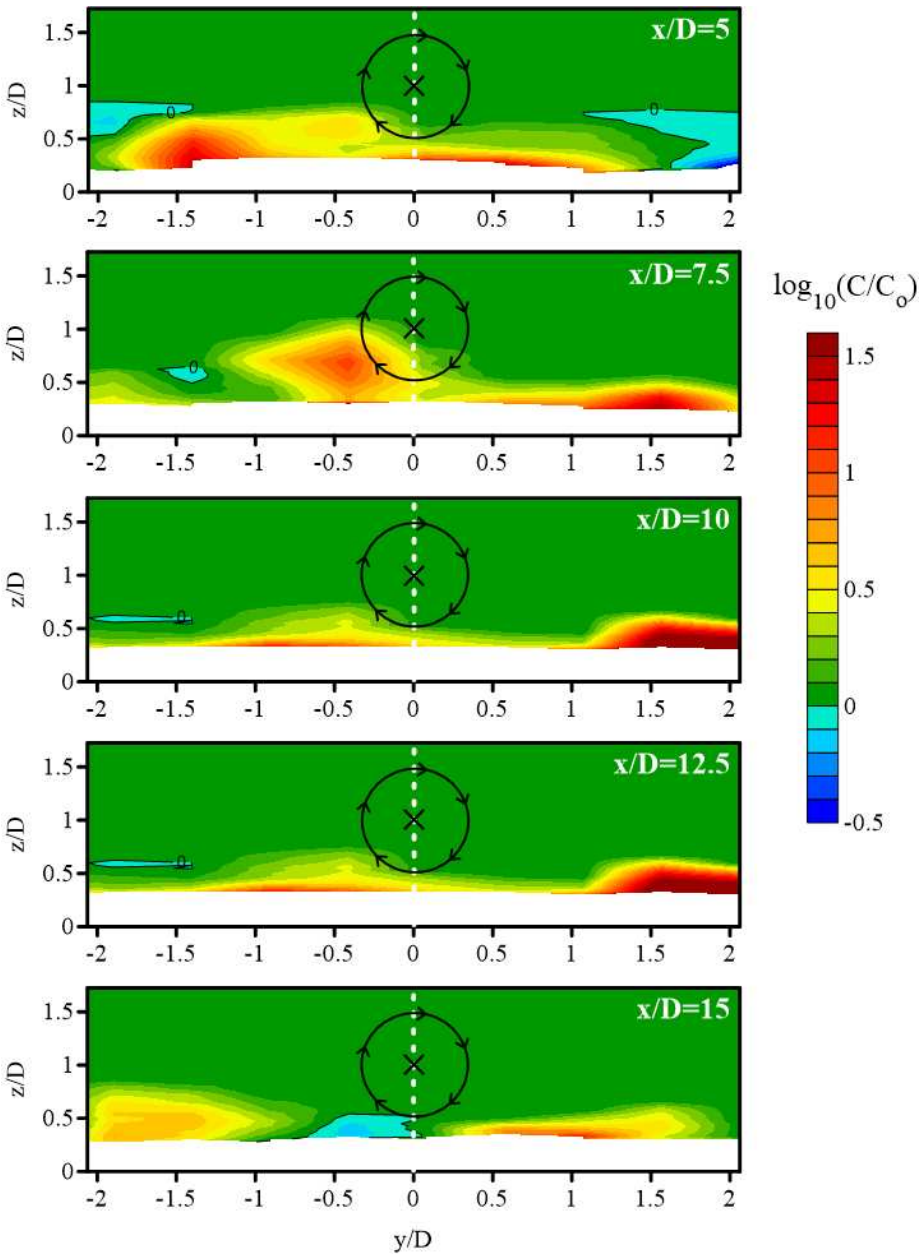

Figure 13: Vertical cross-stream of the base 10 logarithm of the ratio, C/C_o, where C is SSC conditions with rotor and C_o without rotor in the flume. The centreline is marked by the white dashed line at $y/D = 0$, the position of the rotor by the black cross while the black circle with arrows indicates the direction of the rotor gyre.

4. Discussion

Different methods were used in this investigation to examine the asymmetry in the flow and the bed responses, which could be relevant to the deployment of single or arrays of hydrokinetic turbines. Measured and modelled hydrodynamic features showed important differences which increased significantly close to the bed and also impacted asymmetrically on the sediment bed and suspended sediments.

The results show cross-stream asymmetries due to a modification of the flow field because of the presence of the rotor. The flow was greater for $y/D < 0$ than for $y/D > 0$ after $x/D = 1$ according to both numerical modelling and PIV measurements, figures 5 and 8, respectively. This led to a higher turbulent kinetic energy and mixing for $y/D < 0$ than for $y/D > 0$. There was a faster recovery on the $y/D < 0$ which can also be seen in figure 12b where the "V" shape is longer for $y/D > 0$. The effect of the bed shear stress reached a greater area in the streamwise direction (Fig. 6). Far from the rotor, from $x/D = 5$, sediment resuspension is also more effective for $y/D < 0$ which is consistent with modelling results within the domain, $-1 \leq y/D \leq 1$. It is important to note that beyond the model domain there were areas with important SSC mainly at $y/D > 1$ and $5 < x/D < 15$.

The horizontal distribution of the asymmetry in the near-bed flow velocity increases with decreasing the distance between the rotor and the sediment bed (Fig. 5). This result suggests that the relationship between the distance of the turbine from the sediment bed and the excess bed shear stress is strongly influenced by the asymmetry of the turbine wake. Indeed, the close proximity of the sediment bed caused the otherwise ordered helical structure of the wake immediately downstream of the rotor to become skewed resulting in an asymmetric wake near the turbine (i.e. a distortion from a cylindrical structure). An important result from the present study is that the excess bed shear stress when the turbine is placed closer than $z/D = 0.625$ to the sediment bed is influenced by the wake asymmetry as shown in figure 6. Indeed, the ordered

helical vortical structure that induced strong currents when the turbine was placed further above the sediment bed is disrupted by the close vicinity of the sediment bed. The disrupted vortical structure induces an asymmetric velocity field near the sediment bed, effectively reducing the impact of the device on the sediment deposits. In the far wake area there are cross-stream downstream velocity asymmetries, although overall of a smaller magnitude than for the near wake according to numerical modelling (Fig. 5). To a large extent, modelling and experimental results are in qualitative agreement. Nevertheless, some characteristics still need further study, for example the effect of the bed forms (ripples) on the flow field.

Some results of the present investigation are consistent with previous studies. The vortex three-dimensional flow features are similar to those described by Leishman (2006), Pinon et al. (2012), and Mason-Jones et al. (2013). The inclination of the helical structures has been attributed to the effect of the sediment bed (Vybulkova, 2013; Vybulkova et al., 2016), and also to an upward flow behind the turbine (Mason-Jones et al., 2013). Regarding asymmetries, several studies have found clear differences although not much attention has been given to them. Important asymmetries in the downstream shear stress and streamwise velocity were found by Myers and Bahaj (2012) and Tedds et al. (2014), respectively. Slight asymmetries in velocity deficit have also been recorded by Stallard et al. (2013, 2015).

To the present authors knowledge, there is no study focused on asymmetric impacts of TSTs on suspended sediments and sediment bed morphology. Even though some asymmetry can be observed in the results by Hill et al. (2014), their study focused on the scour and in a more recent work on bed form changes at the centreline (Hill et al., 2016). The present study, which we believe to be the first experiments analysing the three dimensional bed changes and three-dimensional sediment resuspension changes due to a TST, complements and extends these earlier reported studies. The results indicate that in the near wake area the bed forms are almost replaced with well-defined scour and deposition areas similar to those found by Hill et al. (2014). Also, the bed form characteristics are

slightly smaller, though comparable, with those by Hill et al. (2016), despite the different experimental setups. Although the experiments were not designed to be an exact scale model, significant features can be found in nature. In terms of the flow, a Re=10^6 is expected in real dimensions. Taking into account a median grain size of about 355 μm, corresponding to the used sand, and the friction velocity reported in Ramírez-Mendoza et al. (2018), the resulting Rouse number of $\sim$2.6 indicates bed load transport which is also expected in a real TST deployment. Therefore, it is considered that the resulted scour and deposition in the near wake area found in the present investigation may develop at full scale. However, as yet there is not the data available to make such a comparison. These findings confirm the need to include sediment transport processes in the entire surrounding area of a TST.

5. Conclusion

The present work combined output from computational fluid dynamics, PIV hydrodynamics, suspended sediments and bed forms observations in order to study the asymmetry due to the presence of a hydrokinetic turbine upon the flow and sediment processes. Taken individually the impact of asymmetry may appear subtle, however, collectively the combination of numerical modelling, PIV flow, suspended sediment and bed form studies provide strong evidence for asymmetry and its impacts. Numerical simulations clearly show a cross-stream difference in streamwise near bed velocity up to a distance of 10 diameters from the turbine. A similar feature was also found using particle image velocimetry measurements in the near wake region and is likely the cause of accretion on one side of the channel and erosion in the other. Additionally, the excess bed shear stress needed for the erosion of the sediment bed was also calculated and showed a maximum for $y/D > 0$ domain in the near wake area, which was also seen in the experiments in the scour behind the rotor. Initial bed forms patterns were altered by the streamwise velocity with the TST present. The smaller velocity magnitude for $y/D > 0$ allowed for the formation of ripples,

while for y/D <0 presented a different distribution. PIV measurements also showed non-symmetrical streamwise velocities mainly near the bed. However, velocity deficit calculations revealed important asymmetries at the height of the rotor and, downstream as far as four rotor diameters. In the far wake area, the sediment resuspension was characterised by localised near bed maxima around y/D=1.5 for y/D>0, while for y/D<0 the location of the near bed maxima was more variable. This pattern could be related to near bed streamwise velocity found in the numerical simulations. Overall, this study shows asymmetries in both flow and sediment dynamics that covered the entire area of the channel bed.

The present study shows the wake asymmetric effects of a hydrokinetic turbine alone. Contrary to the commonly used simplification of regular and uniform characteristics of the flow field or the sediment bed, real deployment sites would exhibit natural spatial heterogeneity, which could enhance asymmetries in both hydrodynamics and sediment dynamics. Another intriguing effect would be the overall result due to an array of TSTs, and how individual asymmetries aggregate and interact. The non-uniform flow could affect TSTs performance located downstream in a similar way to that described for flow asymmetries by Piano et al. (2017). The asymmetric scour patterns have also been identified by Hill et al. (2014) and Chen et al. (2017), but the possible effects on downstream device foundations are still unknown. The impact on the environment due to TSTs arrays has been studied with a numerical model by Ahmadian and Falconer (2012). The authors simulate the TSTs as drag forces and therefore a different result could be expected if the blade rotation effect is taken into account. Our study shows a range of asymmetry features that need further investigation to assess their possible impacts on TSTs performance and the environment.

Acknowledgments

The authors wish to acknowledge funding of the Engineering and Physical Sciences Research Council (EPSRC) to grant EP/J010359 Interactions of flow,

tidal stream turbines and local sediment bed under combined waves and tidal conditions, which is part of the Supergen Consortium, and James Watt Research and EPSRC PhD scholarships. We want to thank Brendan Murphy of the University of Hull for his invaluable help during the experiments in the TES flume.

References

Ahmadian, R., Falconer, R., 2012. Assessment of array shape of tidal stream turbines on hydro-environmental impacts and power output. Renewable Energy 44, 318–327. DOI: 10.1016/j.renene.2012.01.106.

Amoudry, L.O., Souza, A.J., 2011. Deterministic coastal morphological and sediment transport modeling: A review and discussion. Rev. Geophys. 49, 1–21. RG2002, DOI:10.1029/2010RG000341.

Bahaj, A., 2013. Marine current energy conversion: the dawn of a new era in electricity production. Philosofical Transactions of the Royal Society A 371, 1–15. DOI: 10.1098/rsta.2012.0500.

Batten, W., Harrison, M., Bahaj, A., 2013. Accuracy of the actuator disc-RANS approach for predicting the performance and wake of tidal turbines. Philosofical Transactions of the Royal Society A 371, 1–14. DOI: 10.1098/rsta.2012.0293.

Brauns, E., 2009. Salinity gradient power by reverse electrodialysis: effect of model parameters on electrical power output. Desalination 237, 378–391. DOI: 10.1016/j.desal.2008.10.003.

Brown, R., Houston, S., 2000. Comparison of induced velocity models for helicopter flight mechanics. Journal of Aircraft 37, 623–629. DOI: 10.2514/2.2644.

Brown, R., Line, A., 2005. Efficient high-resolution wake modelling using the vortex transport equation. AIAA 43, 1434–1443. DOI: 10.2514/1.13679.

Chamorro, L., Hill, C., Morton, S., Ellis, C., Arndt, R., Sotiropoulos, F., 2013. On the interaction between a turbulent open channel flow and an axial-flow turbine. Journal of Fluid Mechanics 716, 658–670. DOI: 10.1016/j.renene.2017.07.026.

Chen, L., Hashim, R., Othman, F., Motamedi, S., 2017. Experimental study on scour profile of pile-supported horizontal axis tidal current turbine. Renewable Energy 114, 744–754. DOI: 10.1017/jfm.2012.571.

Daly, T., Myers, L., Bahaj, A., 2013. Modelling of the flow field surrounding tidal turbine arrays for varying positions in a channel. Philosofical Transactions of the Royal Society A 371, 1–17. DOI: 10.1098/rsta.2012.0246.

Ellabban, O., Abu-Rub, H., Blaabjerg, F., 2014. Renewable energy resources: Current status, future prospects and their enabling technology. Renewable and Sustainable Energy Reviews 39, 748–764. DOI: 10.1016/j.rser.2014.07.113.

Falnes, J., 2007. A review of wave-energy extraction. Marine Structures 20, 185–201. DOI: 10.1016/j.marstruc.2007.09.001.

Finney, K., 2008. Ocean thermal energy conversion. Guelph Engineering Journal 1, 17–23. ISSN: 1916-1107.

Fletcher, T., Brown, R., 2008. Main-rotor-tail rotor interaction and its implications for helicopter directional control. Journal of the American Helicopter Society 53, 125–138. DOI: 10.4050/JAHS.53.125.

Fletcher, T., Brown, R., 2010. Simulation of wind turbine wake interactions using the vorticity transport model. Wind Energy 13, 587–602. DOI: 10.1002/we.379.

Green, R., Gillies, E., Brown, R., 2005. The flow field around a rotor in axial descend 543, 237–261. DOI: 10.1017/S0022112005004155.

642 Harrison, M., Batten, W., Myers, L., Bahaj, A., 2010. Comparison between
643 CFD simulations and experiments for predicting the far wake of horizontal
644 axis tidal turbines. IET Renewable Power Generation 4, 613–627. DOI:
645 1049/iet-rpg.2009.0193.

646 Hill, C., Musa, M., Chamorro, L., Ellis, C., Guala, M., 2014. Local Scour around
647 a Model Hydrokinetic Turbine in an Erodible Channel. Journal of Hydraulic
648 Engineering 140. DOI: 10.1061/(ASCE)HY.1943-7900.0000900, 04014037.

649 Hill, C., Musa, M., Guala, M., 2016. Interaction between instream axial flow
650 hydrokinetic turbines and uni-directional flow bedforms. Renewable Energy
651 86, 409–421. DOI: 10.1016/j.renene.2015.08.019.

652 Houston, S., Brown, R., 2003. Rotor-wake modeling for simulation of heli-
653 copter flight mechanics in autorotation. Journal of Aircraft 40, 938–945.
654 DOI: 10.2514/2.6870.

655 Jacobs, E., Ward, K., Pinkerton, R., 1935. Report no. 460. "The characteristics
656 of 78 related airfoil sections from tests in the variable-density wind tunnel".
657 Technical Report. National Advisory Committee for Aeronautics.

658 Lee, T., Leishman, J., Ramasamy, M., 2001. Fluid dynamics of interacting
659 blade tip vortices with a ground plane, in: Annual Forum of the Ameri-
660 can Helicopter Society, Journal of the american Helicopter Society. DOI:
661 10.4050/JAHS.55.022005.

662 Leishman, J., 2006. Principles of Helicopter Aerodynamics. Cambridge Univ.
663 Press, Cambridge, UK. Pp. 418-458.

664 Li, X., Li, M., McLelland, S., Jordan, L., Simmons, S., Amoudry, L., Ramírez-
665 Mendoza, R., Thorne, P., 2017. Modelling tidal stream turbines in a three-
666 dimensional wave-current fully coupled oceanographic model. Renewable En-
667 ergy 114, 297–307. DOI: 10.1016/j.renene.2017.02.033.

668 Maganga, F., Germain, G., King, J., Pinon, G., Rivoalen, E., 2010. Experimen-
669 tal characterisation of flow effects on marine current turbine behaviour and

on its wake properties. IET, Renewable Power Generation 4, 498–509. DOI: 10.1049/iet-rpg.2009.0205.

Mason-Jones, A., O'Doherty, D., Morris, C., O'Doherty, T., 2013. Influence of a velocity profile & support structure on tidal stream turbine performance. Renewable Energy 52, 23–30. DOI: 10.1016/j.renene.2012.10.022.

Miller, M., McCave, I., Komar, P., 1977. Threshold of sediment motion under unidirectional current. Sedimentology 24, 507–527. DOI: 10.1111/j.1365-3091.1977.tb00136.x.

Moate, B., Thorne, P., Cooke, R., 2016. Field deployment and evaluation of a prototype autonomous two dimensional acoustic backscatter instrument: The Bedform And Suspended Sediment Imager (BASSI). Continental Shelf Research 112, 78–91. DOI: 10.1016/j.csr.2015.10.017.

Möller, N., Kim, H., Neary, V., García, M., Chamorro, L., 2016. On the near-wall effects induced by an axial-flow rotor. Renewable Energy 91, 524–530. DOI: 10.1016/j.renene.2016.01.05.

Myers, L., Bahaj, A.S., 2005. Simulated electrical power potential harnessed by marine current turbine arrays in the alderney race. Renewable Energy 30, 1713–1731. DOI: 10.1016/j.renene.2005.02.008.

Myers, L., Bahaj, A.S., 2010. Experimental analysis of the flow field around horizontal axis tidal turbines by use of scale mesh disk rotor simulators. Ocean Engineering 37, 218–227. DOI: 10.1016/j.oceaneng.2009.11.004.

Myers, L., Bahaj, A.S., 2012. An experimental investigation simulating flow effects in first generation marine current energy converter arrays. Renewable Energy 37, 28–36. DOI: 10.1016/j.renene.2011.03.043.

Olczak, A., Sudall, D.and Stallard, T., Stansby, P., 2015. Evaluation of rans bem and self-similar wake superposition for tidal stream turbine arrays, in: Proceedings of the 11th European Wave and Tidal Energy Conference, 6th-11th Sept. 2015, Nantes, France.

Phillips, C., 2010. Computational study of rotorcraft aerodynamics in ground effect and brownout. Ph.D. thesis. University of Glasgow. United Kingdom.

Piano, M., Neill, S., Lewis, M., Robins, O., Davies, A., Ward, S., Roberts, M., 2017. Tidal stream resource assessment uncertainty due to flow asymmetry and turbine yaw misalignment. Renewable Energy 114, 1363–1375. DOI: 10.1016/j.renene.2017.05.023.

Pinon, G., Mycek, P., Germain, G., Rivoalen, E., 2012. Numerical simulation of the wake of marine current turbines with a particle method. Renewable Energy 46, 111–126. DOI: 10.1016/j.renene.2012.03.037.

Prandle, D., 1982. The vertical structure of tidal currents and other oscillatory flows. Continental Shelf Research 1, 191–207. DOI: 10.1016/0278-4343(82)90004-8.

Ramírez-Mendoza, R., Amoudry, L., Thorne, P., Cooke, R., McLelland, S., Jordan, L., Simmons, S., Parsons, D., Murdoch, L., 2018. Laboratory study on the effects of hydro kinetic turbines on hydrodynamics and sediment dynamics. Renewable Energy 129, 271 – 284. DOI: 10.1016/j.renene.2018.05.094.

Reineck, H., Singh, I., 1975. Depositional Sedimentary Environments: With Reference to Terrigenous Clastics. ISBN 3540073779, 9783540073772.

van Rijn, L.C., 2007. Unified view of sediment transport by currents and waves. I: Initiation of motion, bed roughness, and bed load transport. Journal of Hydraulic Engineering 133, 649–667. DOI: 10.1061/(ASCE)0733-9429(2007)133:6(649).

Roc, T., Conley, C., Greaves, D., 2013. Methodology for tidal turbine representation in ocean circulation model. Renewable Energy 51, 448–464. DOI: 10.1016/j.renene.2012.09.039.

Scheurich, F., Brown, R., 2011. Effect of dynamic stall on the aerodynamics of vertical-axis wind turbines. AIAA Journal 49, 2511–2521. DOI: 10.2514/1.J051060.

Scheurich, F., Fletcher, T., Brown, R., 2011. Simulating the aerodynamic performance and wake dynamics of a vertical-axis wind turbine. Wind Energy 14, 159–177. DOI: 10.1002/we.409.

Simmons, S., McLelland, S., Parsons, D., Jordan, L., Murphy, B., Murdoch, L., 2018. An investigation of the wake recovery of two model horizontal-axis tidal stream turbines measured in a laboratory flume with particle image velocimetry. Journal of Hydro-environment Research 19, 179–188. DOI: 10.1016/j.jher.2017.03.003.

Stallard, T., Collings, R., Feng, T., Whelan, J., 2013. Interactions between tidal turbine wakes: experimental study of a group of three-bladded rotors. Phylosophical Transactions of the Royal Society A 371, 1–13. DOI: 10.1098/rsta.2012.0159.

Stallard, T., Feng, T., Stansby, P., 2015. Experimental study of the mean wake of a tidal stream rotor in a shallow turbulent flow. Journal of fluids and structures 54, 235–246. DOI: 10.1016/j.jfluidstructs.2014.10.017.

Tatum, S., Allmark, M., Frost, C., O'Doherty, D., Mason-Jones, A., O'Doherty, T., 2016. CFD modelling of a tidal stream turbine subjected to profiled flow and surface gravity waves 15, 156–174. DOI: 10.1016/j.ijome.2016.04.003.

Tedds, S., Owen, I., Poole, R., 2014. Near-wake characteristics of a model horizontal axis tidal stream turbine. Renewable Energy 63, 222–235. DOI: 10.1016/j.renene.2013.09.011.

Theunissen, R., Scarano, F., Riethmuller, M.L., 2007. An adaptive sampling and windowing interrogation method in PIV. Measurement Science Technology 18, 275–287. DOI: 10.1088/0957-0233/18/1/034.

Thiébot, J., Bailly du Bois, P., Guillou, S., 2015. Numerical modelling of the effect of tidal stream turbines on the hydrodynamics and the sediment transport - Application to the Alderney Race (Raz Blanchard), France. Renewable Energy 75, 356–365. DOI: 10.1016/j.renene.2014.10.21.

754 Thorne, P., Meral, R., 2008. Formulations for the scattering properties of
755 suspended sandy sediments for use in the application of acoustics to sedi-
756 ment transport processes. Continental Shelf Research 28, 309–317. DOI:
757 10.1016/j.csr.2007.08.002.

758 Thorne, P.D., Hurther, D., Cooke, R.D., Caceres, I., Barraud, P., Sánchez-
759 Arcilla, A., 2018. Developments in acoustics for studying wave-driven bound-
760 ary layer flow and sediment dynamics over rippled sand-beds. Continental
761 Shelf Research 166, 119 – 137. DOI: 10.1016/j.csr.2018.07.008.

762 Vybulkova, L., 2013. A study of the wake of an isolated tidal turbine with
763 application to its effects on local sediment transport. Ph.D. thesis. University
764 of Glasgow. United Kingdom.

765 Vybulkova, L., Vezza, M., Brown, R., 2016. Simulating the wake down-
766 stream of a horizontal axis tidal turbine using a modified vorticity trans-
767 port model. IEEE Journal of Oceanic Engineering 41, 296–301. DOI:
768 10.1109/JOE.2015.2429231.

769 Whitehouse, G., Brown, R., 2004. Modelling rotor wakes in ground ef-
770 fect. Journal of the American Helicopter Society 49, 238–249. DOI:
771 10.4050/JAHS.49.238.